ACS APPLIED MATERIALS & INTERFACES

Research Article

Cite This: ACS Appl. Mater. Interfaces XXXX, XXX, XXX−XXX

www.acsami.org

Thermal Reshaping of Gold Microplates: Three Possible Routes and Their Transformation Mechanisms

Rui Wang[†] and Dmitry Kurouski*[,†,‡]

[†]Department of Biochemistry and Biophysics and [‡]The Institute for Quantum Science and Engineering, Texas A&M University, College Station, Texas 77843, United States

Supporting Information

ABSTRACT: The thermal stability of Au micro/nanomaterials (AuMNLs) has always been a hot topic because their physicochemical properties, like surface plasmon resonance and catalytic activity, are closely related to their morphology or exposed crystal planes which are heat-sensitive. In this study, we made careful and systematic investigation of thermal deformation and reshaping of individual Au microplates (AuMPs) using atomic force microscopy. We found that AuMPs could transform into walled AuMPs (WAuMPs) and concave AuMPs (CAuMPs) at just 300 °C, which are thermodynamically and kinetically favorable products, respectively. A small fraction of AuMPs, named invariable AuMPs (IAuMPs), remained intact. However, both CAuMPs and IAuMPs can be converted to WAuMPs if the temperature is further increased. We also showed that melting of AuMPs begins from vertices and the boundaries between the top and side plane, rather than only side crystal planes as envisaged before. Finally, we performed a series of electrochemical studies showing that WAuMPs exhibited substantially higher electrocatalytic conversion of methanol at lower formal potential compared to intact AuMPs. This work shows that thermal reshaping of Au is far more complicated as was expected before. It also demonstrates how thermal reshaping can be used to improve electrocatalytic performance of Au and potentially other MNLs.

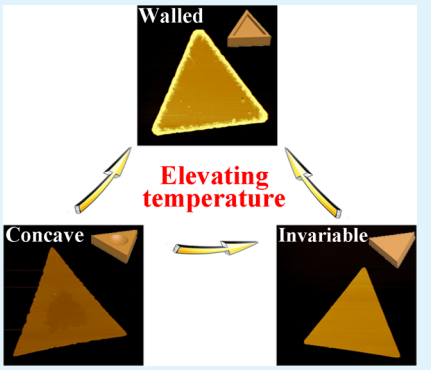

KEYWORDS: *Au microplates, thermal stability, reshaping mechanism, electrochemical catalysis, AFM*

INTRODUCTION

Au micro/nanomaterials (AuMNLs) have attracted extensive attention because of their potential applications in different fields, including bioimaging,[1−3] drug delivery,[4−6] data storage,[7] and catalysis.[8−10] With certain crystal facets exposed or anisotropic morphology formed, they exhibit many unique physicochemical properties, such as surface plasmon resonance (SPR)[11−14] and facet-dependent catalysis.[15−17] However, SPR generates a large amount of heat, and many catalytic reactions occur at high temperatures, both of which cause deformation and reshaping of AuMNL, thereby losing activity.[18−22] Therefore, understanding the thermal stability and reshaping mechanism of AuMNLs is highly important. Until now, many efforts have been devoted to investigating the thermal reshaping behavior of Au nanomaterials.[23−26] It was observed that the melting point of Au nanoparticles (Au NPs) is strongly associated with their size. For example, the melting temperature of 5 nm Au NPs drops sharply from 1100 to 600 K when their sizes decrease to 2 nm.[27] Moreover, the AuMNLs prone to sintering after melting follow two mechanisms: (1) Ostwald ripening, which involves small crystals or clusters dissolving and redepositing onto larger crystals; (2) particle migration and coalescence involving spontaneous Brownian motion and fusion of particles.[28−30]

Au micromaterials are generally considered to have higher thermal stability than Au nanomaterials because of their larger size and smaller surface free energy.[31−33] However, recent studies have shown that some Au micromaterials, such as Au microplates (AuMPs), also undergo deformation and reshaping at temperatures much below the melting point of bulk Au (1337 K).[34] Kan et al.[35] found the fragmentation behavior of AuMPs when the heating temperature is above 450 °C, which can be attributed to the fact that the melting point of the side facets ({110}) is lower than that of the top facets ({111}). Independently, Kulkarni and Radha[36] found that AuMPs could build up high edges upon heating. The researchers proposed that such reshaping could be caused by migration of Au atoms from the center outwards to the edges of AuMPs. These findings show that heat-induced transformations in Au micromaterials are very sophisticated. Also, it becomes evident that there is no clear understanding about possible reshaping routes of AuMPs, the relating factors and transformation mechanism of AuMPs.

In this study, we made careful and systematic investigation of the thermal deformation and reshaping of AuMPs. We used atomic force microscopy (AFM) to monitor transformations in individual AuMPs heated at 300, 400, and 500 °C. We found that AuMPs could be transformed into walled AuMPs

Received: August 29, 2019
Accepted: October 15, 2019
Published: October 15, 2019

DOI: 10.1021/acsami.9b15600
ACS Appl. Mater. Interfaces XXXX, XXX, XXX−XXX

(WAuMPs) and Concave AuMPs (CAuMPs) (Scheme 1), the thermodynamic and kinetic products of AuMPs reshaping, respectively. With prolonged heating, the WAuMPs were gradually deformed and fragmented, which is similar to the observation made by Kan and co-workers.[35] Some of the AuMPs remained intact [invariable AuMPs (IAuMPs)] upon heating. Neverthelss, CAuMPs and IAuMPs could be converted to WAuMPs at elevated temperatures (Scheme 1). The appearance of WAuMPs is similar with Kulkarni's finding,[36] however, by using the magnitude-mode AFM and high-resolution AFM (HRAFM), we found that WAuMPs were formed by shrinking from the edge to the interior, rather than as Kulkarni speculated. The HRAFM also showed that the walls of the WAuMPs are made of many ultrathin (~2 nm) layered structures. One explanation for these phenomena is that the melting of AuMPs actually begins at the vertices and the boundaries between the top and side plane, rather than only the side crystal plane as envisaged before. Finally, we found that WAuMPs exhibited much higher electrocatalytic activity (119.7 μA cm^{-2}) than that of intact AuMPs (67.1 μA cm^{-2}) in the methanol oxidation reaction, which can be attributed to their unique nanosized layered structures on the walls.

Scheme 1. Three Possible Thermal Reshaping Routes of AuMPs upon Calcination at a Certain Temperature

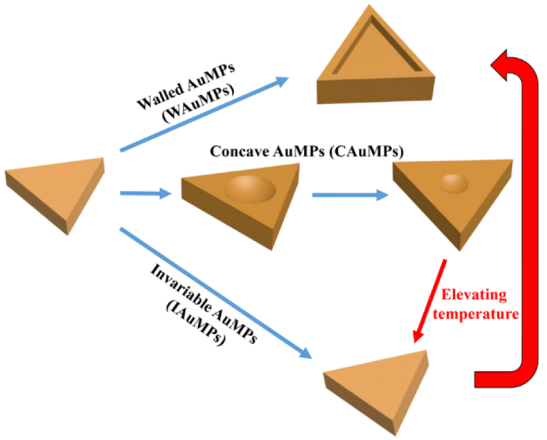

RESULTS AND DISCUSSION

Three Possible Thermal Transformation Routes of AuMPs and Their Affecting Factors. The AuMPs were synthesized according to a "wet-chemical" protocol.[37] The as-made AuMPs were generally hexagonal and triangular microplates with 15−35 μm in length. Two groups of AuMPs with different thickness: 30 ± 10 nm (30 nm group) and 60 ± 20 nm (60 nm group) were synthesized by controlling the adding amount of the polyvinyl pyrrolidone (PVP), a surfactant which can reduce the growth rate of basal planes, but enhance those of lateral planes. After drop casting on precleaned Si wafer, AFM images of a specific piece of AuMP were taken both before and after calcination. Figure 1a−d shows a representative WAuMP growth results: the selected 30 nm group AuMP started the "wall building" process which showed a higher edge than the interior after 400 °C calcination. As the calcination time increased from 30 to 120 min, the wall height increased from 23 to 40 nm. Meanwhile, after calcination for 30 and 120 min, the average length of the AuMP was also shortened by 1.3 and 2.4 μm, respectively, compared with that of the corresponding as-made AuMP. In contrast, the thickness of the interior of the AuMP changed little during the whole process, indicating that the deformation and reshaping only starts from the edge of the WAuMPs. The beginning of CAuMP growth is quite similar: the walls were generated and the AuMP experienced a slight shrink (~0.5 μm) after 30 min of heating (Figure 1e−h), creating a concave structure with a 2−4 nm thick hole in the

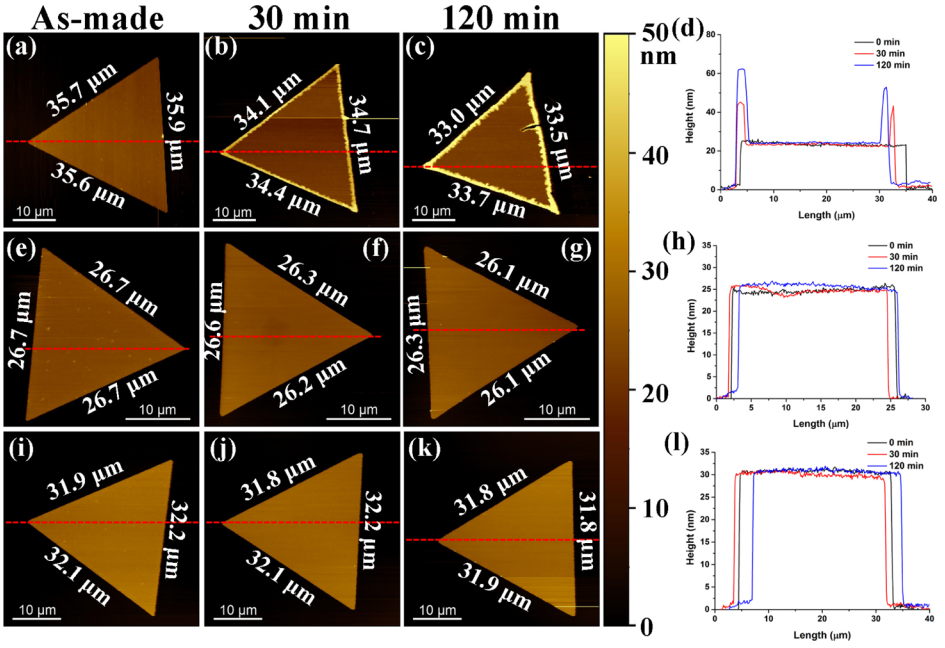

Figure 1. Representative AFM images of WAuMPs (b,c), CAuMPs (f,g), and IAuMPs (j,k) formed by the 30 nm group calcinated at 400 °C for different times and their corresponding as-made AuMPs (a,e,i), respectively. (d,h,l) are the corresponding height profile along the red dashed line in (a−c), (e−g), and (i−k), respectively.

DOI: 10.1021/acsami.9b15600
ACS Appl. Mater. Interfaces XXXX, XXX, XXX−XXX

center. However, instead of building up the wall and shrinking further as WAuMPs do, the hole was re-filled and the resulting CAuMPs had similar appearance with the as-made ones. Because of their opposite growth performance, products with a "wall" height less than 5 nm and width wider than 5 μm are defined as CAuMPs, and the converse would be WAuMPs. Besides WAuMPs and CAuMPs, we found the rest AuMPs with both thickness and length maintained after 400 °C calcination for the 30 nm group, denoted as IAuMPs. One can expect that these IAuMPs have higher transformation threshold than those of WAuMPs and CAuMPs. This hypothesis will be verified in the experiment that will be discussed below. For the 60 nm group, we also found the same reshaping pathways, that is, WAuMPs, CAuMPs, and IAuMPs, after 400 °C calcination (Figure S1), except that the formation of CAuMPs was slower (Figure S2) than that of the 30 nm group.

To further understand the factors affecting the deformation and reshaping routes of AuMPs, the thermal stability tests for both 30 and 60 nm groups were conducted at different temperature (300, 400, and 500 °C). For each group calcinated at a certain temperature, 25 pieces of AuMPs were unbiasedly chosen and traced by AFM imaging. As shown in Figures S3–S5, Tables 1 and 2, we can see that a part of the

Table 1. The Percentage of Different Thermal Products of the 30 nm Group after Calcination at Different Temperatures for 2 h[a]

	300 °C (%)	400 °C (%)	500 °C (%)
WAuMPs	52	68	96
CAuMPs	4	8	4
IAuMPs	44	24	0

[a]Extracted from Figures S3, S6, S7.

Table 2. The Percentage of Different Thermal Products of the 60 nm Group after Calcination at Different Temperatures for 2 h[a]

	300 °C (%)	400 °C (%)	500 °C (%)
WAuMPs	0	40	92
CAuMPs	0	12	0
IAuMPs	100	48	8

[a]Extracted from Figure S3, S6, S7.

30 nm group AuMPs have grown 2–5 nm walls after 300 °C calcination, which is a clear sign of WAuMPs reshaping, while 60 nm group AuMPs were still intact even after 120 min. When the calcination temperature was brought up to 400 °C, the ratio of WAuMPs in the 60 nm group (10 out of 25) increased, but still much less than that of the 30 nm group (17 out of 25) (Figures 1, S1, S6 and Tables 1 and 2); and after 500 °C heating, most of them were transformed to WAuMPs or CAuMPs (Figures S7–S9, Tables 1 and 2). Based on the above findings, it can be expected that the thermal stability of the 60 nm group is higher than that of the 30 nm group, that is, thicker AuMPs lead to higher thermal stability.

Further Conversion among Different Reshaping Products. Next, we studied the conversion possibility among these three reshaping products. With prolonged heating at a certain temperature (400 °C), CAuMPs would fill the holes and become IAuMPs (Figure 2a–d,f–i). Surprisingly, their edges became higher with further temperature increase to 500 °C and they either turned into WAuMPs (Figure 2a–e) or started a new round of CAuMPs growth (Figure 2f–j). Similarly, IAuMPs could also be converted to WAuMPs at higher temperatures (Figure 2k–o). These results indicate that CAuMPs and IAuMPs are more unstable and can be converted to WAuMPs at higher temperatures, which is consistent with our hypothesis: WAuMPs and CAuMPs are thermodynamically and kinetically controlled products, respectively, and IAuMPs are species with higher transformation threshold. Besides the conversion of CAuMPs and IAuMPs, we also observed that after prolonged heating, some of these WAuMPs could be disintegrated into mesh structures (Figure S10a–j). The explanation for this phenomenon is that the interior of AuMPs begins to deform and rupture because of uneven heating, thus becoming a new reshaping and growth starting point. Besides that, optical images (Figure S11) show that the golden color of AuMPs would be maintained throughout the heating up to 500 °C, but would be dramatically changed at 800 °C, which corresponds to the fully deformed to mesh structures (Figure S11e,f).

Nanostructures on the WAuMPs. In order to unravel the nature of the walls in WAuMPs, we applied magnitude-mode AFM to measure them. Compared to the previously used height mode AFM, magnitude-mode AFM is more sensitive to changes in the hardness of the sample, such as from the silicon substrate to the gold sample surface. As shown in Figure 3, we can see the obvious shrinkage residues of WAuMPs on both low magnification (Figure 3b) and zoomed-in magnitude-mode AFM (Figure 3d), and the shrink of the vertices are even more pronounced than the edges. However, these phenomena were not seen on the corresponding height mode AFM (Figure 3a,c). Furthermore, we studied the evolution of the wall as the heating time changes using HRAFM (Figure 4). The edge and interior of AuMPs did not show significant differences before heating (0 min, Figure 4a–d). After heating at 500 °C for 30 min (Figure 4e–h), the edges turned into layered structures with ~1 nm thickness, but the interior was still flat. As the heating time increases, the layered structure gradually thickened to ~1.5 nm (2 h, Figure 4i–l) and ~3 nm (6 h, Figure 4m–p), while the middle remained stable. Combined with the fact that the edges of AuMPs shrinked, we can infer that the gold atoms at the edges would become unstable during heating and migrate inward, followed by gradually cooling to form layered structures. This is particularly significant at the vertices, which may relate to their lower coordination number and higher surface energy and therefore more thermally unstable.

Another interesting finding is that the surface of these AuMPs, both edge and interior, are covered with small NPs, which were not found either by scanning electron microscopy (SEM) (Figures S12, S13) or high-resolution transmission electron microscopy (TEM) (Figure S14) imaging. This suggests that they have organic rather than metallic nature. Further analysis of these NPs revealed that the particle size was 1–2 nm before calcination (Figure 4d), and increased to ~3 nm (Figure 4h) after calcination at 500 °C, and did not grow further with continuous calcination (Figure 4i,p). In order to exclude the image artifacts brought by the AFM probes, two brand new AFM probes with different tip types (standard T type and pyramid-like tip) were used for HRAFM imaging of the same area. As shown in Figure S15, the two HRAFM images are identical, and the measured particle sizes are also very close, indicating these NPs are real, instead of artifacts. Moreover, we found that when these WAuMPs were stored for

DOI: 10.1021/acsami.9b15600
ACS Appl. Mater. Interfaces XXXX, XXX, XXX–XXX

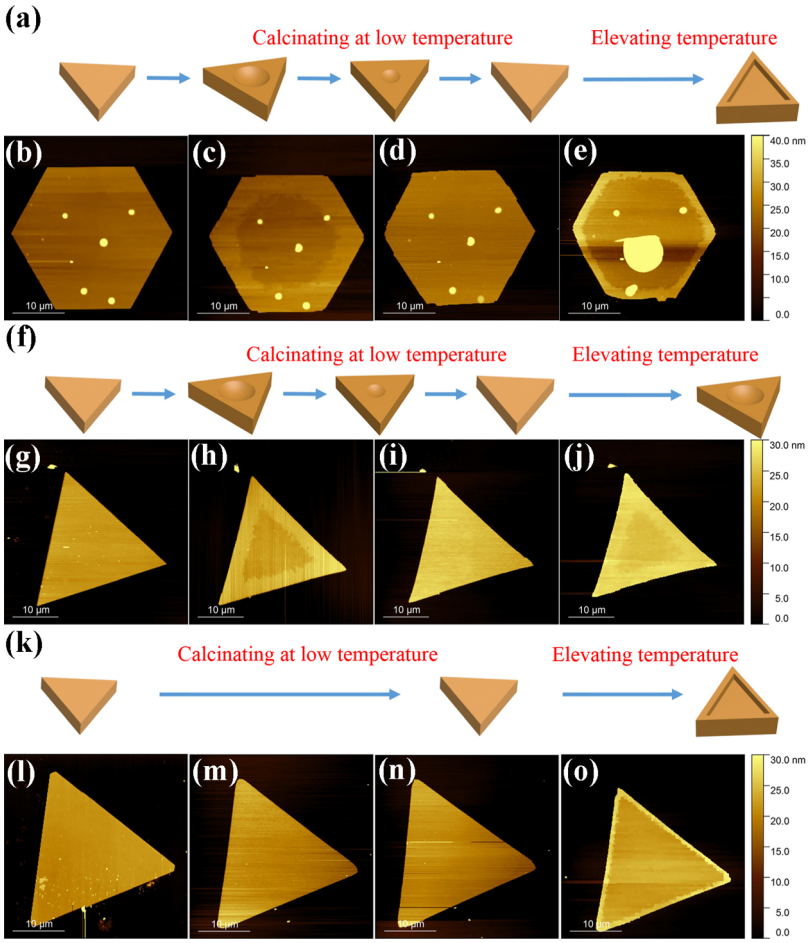

Figure 2. Schemes (a,f,k) and AFM images (b−e,g−j,l−0) of the forming processes of CAuMPs (b−d,g−i) and IAuMPs (l−n) at 400 °C for 0 min (b,g,l), 30 min (c,h,m), and 120 min (d,I,n), followed by corresponding transformation at 500 °C for 2 h (e,j,o).

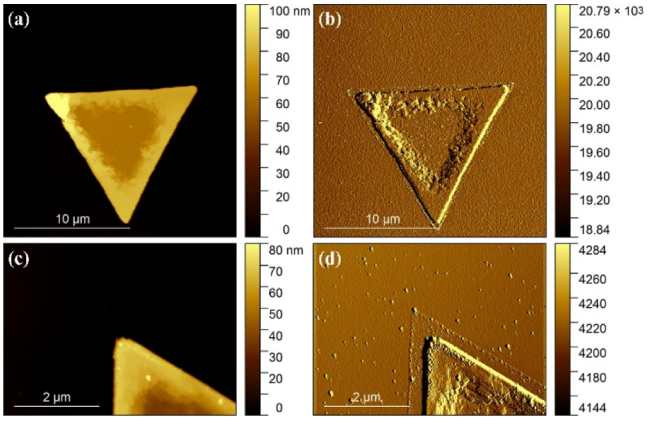

Figure 3. Height-mode (a,c) and magnitude-mode (b,d) AFM images of WAuMPs (500 °C, 120 min) at low (a,b) and high (c,d) magnification.

1 year, the surface NPs would continue to grow to 10−20 nm (Figure S16a,b). After washing with a piranha solution, these NPs disappeared and the surface of WAuMPs became flat (Figure S16c,d), indicating that these NPs are highly likely to be surfactant residues, which are prone to aggregate slowly. To confirm the nature of these small NPs, we conducted the energy dispersion spectrum analysis (Figure S17) on both as-made AuMPs and WAuMPs (formed after 500 °C calcination for 2 h). On both samples, we found the existence of C, O, and Br which can be assigned to PVP and hexadecyltrimethylammonium bromide (CTAB) used during the synthesis along with the Au. The atomic elementary ratio (C/O/Br/Au) was reduced from 4.0:0.5:0.5:1 to 1.7:0.2:0.3:1, indicating that the calcination is not capable to remove the organic species entirely, which can thereafter construct the NPs.

Formation Mechanisms of the Thermal Transformation of AuMPs. In the study of the thermal stability of AuMNLs, it is usually found that the melting phenomenon occurs only at the {110} crystal facets, while the {111} facets remain crystallized until and even higher than the melting point.[26,38] For instance, surface melting starts at ∼500 °C for {111} oriented gold structures, as reported before. Kan et al.[35] discovered that the deformation and cracking of the AuMPs begins with the edges that can be assigned to Au {110} facets. However, based on our above results, the deformation and reshaping process of AuMPs is much more complicated. Based on our results, we hypothesize that thermal reshaping of {110} facets first begins from Au atoms located in vertices and boundaries (between the side and top facets). Possessing high kinetic energy, these Au atoms move inward (Scheme 2a).[9] After the top atoms on the surface have migrated, the atoms beneath them (still belong to {110} facets) become new vertices and boundaries. We hypothesize that WAuMPs and CAuMPs undergo different evolutionary processes after this step. WAuMPs appear as a result of the thermodynamically controlled growth. Specifically, the external energy is much

DOI: 10.1021/acsami.9b15600
ACS Appl. Mater. Interfaces XXXX, XXX, XXX−XXX

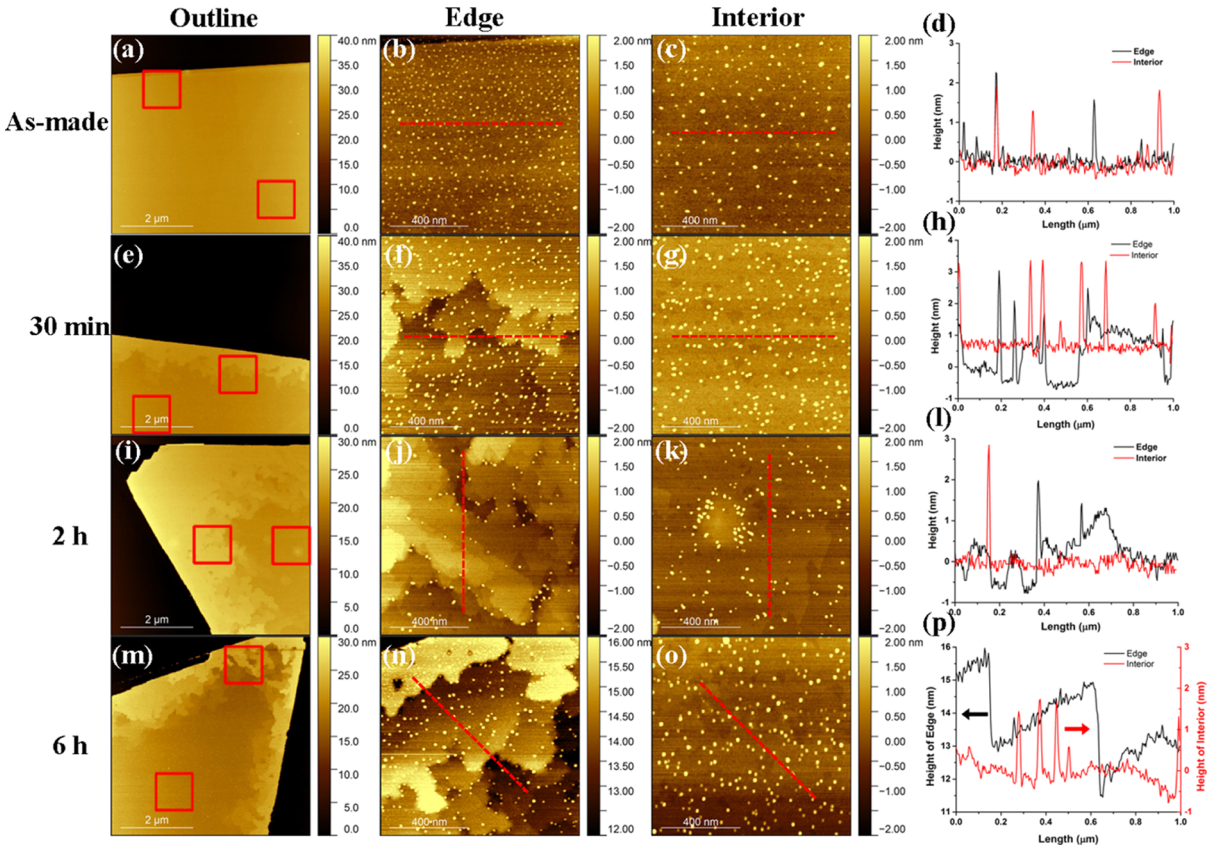

Figure 4. HRAFM images of the "wall" structure of the WAuMPs formed by calcination at 500 °C for different times: 0 min (a−c), 30 min (e−g), 2 h (i−k), and 6 h (m−o). The red rectangles in (a,e,I,m) represent the edge and interior areas where the zoomed-in HRAFM images (b,c), (l,g), (j,k), and (n,o) were taken from, respectively. (d,h,l,p) Corresponding height profile along the red dashed line in (b,c), (l,g), (j,k), and (n,o), respectively.

Scheme 2. (a) Proposed Transformation Mechanism of WAuMPs and CAuMPs upon Heating. (b) The Energy Diagram Regarding the Reshaping Process

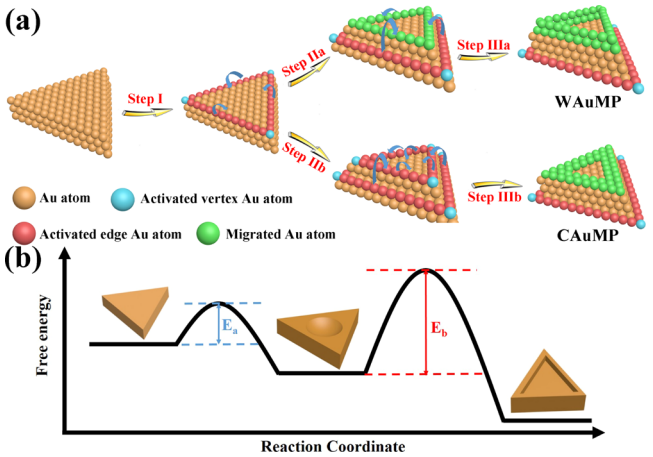

higher than both activation energy E_a and E_b (Scheme 2b) and the atom migration proceeds faster, leading to rapid "wall" generation (Step IIa and Step IIIa). At the same time, in the case of CAuMPs, which appear as a result of kinetically controlled growth, the external energy can only overcome E_a (Scheme 2b). Therefore, besides the new vertex and boundary atoms, the newly generated wall atoms will be activated again and migrate further inward slowly (Step IIb). This will first result in the formation of a hole. Next, this hole will be filled up gradually to reach a new stable structure (Step IIIb). When the temperature is elevated, CAuMPs can also further convert to WAuMPs (Figure 2a−e) when the energy is enough for it to pass E_b (Scheme 2b). These principles also apply to IAuMPs, which have higher transformation thresholds (Figure 2k−o). It should be noted that the transformation threshold temperature appears to be an intrinsic property of AuMPs and has little to do with their shape. In order to prove that the WAuMPs formation is only an manner of "surface melting", rather than gravity affected "direct melting", we calcinated the AuMPs with a substrate slant by 45°. The formation of WAuMPs was still found, and the width of the sides of the wall was not correlated with the substrate tilt direction (Figure S18), which proved that the formation was independent of gravity. Furthermore, we confirmed the AuMPs with 5−15 μm in length can also be transformed to WAuMPs upon heating at 500 °C for 2 h (Figure S19), indicating that the WAuMPs transformation can also be applied to smaller AuMPs. Moreover, in order to study the relevance between the WAuMPs and their plasmonic property, we measured the absorption spectra (Figure S20) of the 30 nm group AuMPs before and after calcination at 300, 400, and 500 °C for 2 h, respectively. For the as-made and 300 °C calcined AuMPs, we can clearly observe an absorption peak located at ∼1100 nm, which corresponds to the in-plane dipole resonance mode of the AuMPs.[39] However, this peak disappeared after 400 and 500 °C calcination, which corresponds to the massive formation of WAuMPs (yield 68 and 96%, respectively, Table 1). In other words, the WAuMPs are not as plasmonic active as their as-made counterparts. We

DOI: 10.1021/acsami.9b15600
ACS Appl. Mater. Interfaces XXXX, XXX, XXX−XXX

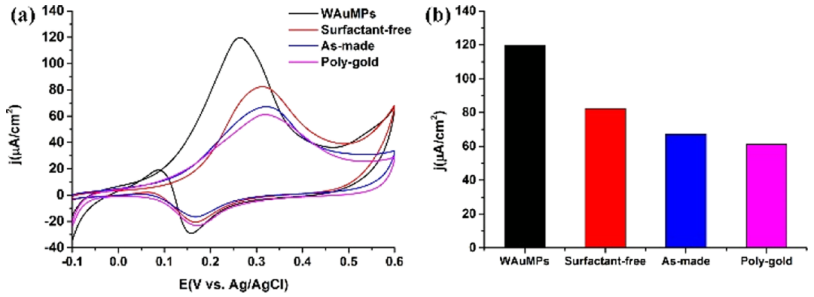

Figure 5. CVs (a) and calculated current density (b) for methanol oxidation at WAuMPs, surfactant-free, as-made and poly-gold electrodes. Scan rates are 10 mV s^{-1}.

hypothesized that the "wall" formation actually is a kind of distortion process to the vertices and edges, where the plasmonic property comes from. Until now, we have only confirmed that their thickness is a vital parameter for the generation of WAuMPs, which may affect the transformation threshold temperature. At the same time, it is still impossible to predict the type of reshaping of a particular AuMP prior to calcination. We hypothesize that this may only be related to the local properties of AuMPs, that is, unstable vertices and boundaries because the deformation and reshaping we observed are confined to edges and far below the melting point.

Electrocatalysis Study of WAuMPs. Previously, it has been reported that AuMNLs exhibit strong electrochemical catalytic activity.[40−42] The question to ask is whether thermally reshaped WAuMPs would have different electrocatalytic activities compared to the intact AuMPs. To answer this question, we investigated electrocatalytic properties of WAuMPs (formed at 500 °C) for the electrocatalytic oxidation of methanol. WAuMPs were deposited on the top of a commercial glassy carbon electrode. The same electrode deposited with intact AuMPs was used as a reference. However, one could note that intact AuMPs may have a surfactant present on their surface. To avoid the contribution of surfactant-masked areas of AuMPs, we prepared surfactant-free AuMPs by treating intact AuMPs in a UV−ozonator. Moreover, a standard Au electrode (poly-gold) was mechanically cleaned followed by activation to serve as a reference, too. Cyclic voltammograms (CV) were obtained for all electrodes in 0.1 M KOH (Figure S21). An oxidation wave located at 0.32 V and a reduction peak at ∼0.16 V were observed, which can be assigned to the formation of surface oxides and their reduction process, respectively. The surface area of WAuMPs, surfactant-free AuMPs, and as-made AuMPs-modified glassy carbon electrodes was calculated to be 0.015, 0.029, and 0.011 cm^2, respectively, from the charge consumed when reducing surface oxides on clean Au electrodes using the reported value of 400 $\mu C\ cm^{-2}$ (see Methods). We have found that anodic waves became broader and larger for all of the electrodes upon addition of 1 M methanol to the electrolyte, indicating oxidation of methanol (Figure 5a). We found that the peak current density of WAuMP electrodes (119.7 $\mu A\ cm^{-2}$) was significantly higher than that of intact AuMP (67.1 $\mu A\ cm^{-2}$), surfactant-free AuMP (82.3 $\mu A\ cm^{-2}$), and poly-gold (61.2 $\mu A\ cm^{-2}$) electrodes (Figure 5b). This indicates that WAuMPs have significantly higher electrocatalytic activity toward methanol oxidation comparing to intact and surfactant-free AuMPs. Moreover, the formal potential of the oxidation peak of WAuMPs (0.265 V) was also much lower than the rest of the samples (∼0.33 V), indicating that WAuMPs are capable to oxidize methanol at much lower formal potential than intact, surfactant-free AuMPs and poly-gold. One can envision that such enhancement in the electrocatalytic activity of WAuMPs can be explained by the unique "wall" architecture of these nanostructures. Additional studies are required to fully understand the structure−catalytic activity relationship of WAuMPs.

CONCLUSIONS

In conclusion, we investigated three possible thermal reshaping routes of AuMPs. Two of them lead to a formation of WAuMPs and CAuMPs which are the products of thermodynamic and kinetic transformations of AuMPs, respectively. The third route does not produce morphologically different structures suggesting that IAuMPs have higher transformation threshold. This hypothesis is supported by the observation that at higher temperatures CAuMPs and IAuMPs can be converted into WAuMPs. We also found that a yield of WAuMPs was determined by the thickness of AuMPs and the heating temperature. We also showed that WAuMPs were formed by migration of Au atoms inwards from the edges to the center of the plate. Based on the above facts, we proposed a new model of thermal reshaping of AuMPs. According to this model, Au atoms located in boundaries of AuMPs are activated first. Their high kinetic energies slowly decrease as they move inwards. This energy-driven migration of atoms results in the appearance of walls at the edges of AuMPs. We also showed that these unique architectures exhibit much higher electrocatalytic methanol oxidation activities compared to intact AuMPs.

METHODS

Chemicals. Diethylene glycol (DEG, 99%), polyvinylpyrrolidone (PVP, average molecular weight 40 000), hexadecyltrimethylammonium bromide (CTAB, 98%), gold (III) chloride trihydrate ($HAuCl_4 \cdot 3H_2O$, 99.9%), potassium hydroxide (KOH, 86%), and Nafion 117 solution (∼5%) were bought from Sigma-Aldrich (St. Louis, MO). Ethanol was obtained from Decon Labs (King of Prussia, PA). Anhydrous methanol (CH_3OH), hydrogen peroxide (H_2O_2, ∼30%), and sulfuric acid (H_2SO_4) were bought from Avantor (Center Valley, PA). No further purification was conducted for all chemicals.

AuMPs Synthesis. A typical synthesis of AuMPs with a thickness of 30 ± 10 nm was carried out as follows. 112 mg of CTAB and 512 mg of PVP were dissolved in 7.2 mL of DEG at 150 °C in a sealed flask. Meanwhile, a stock solution containing 9.6 mg of $HAuCl_4 \cdot 3H_2O$ and 0.8 mL of DEG was prepared. The above stock solution was injected into the flask and maintained at 150 °C for 5 min. Then, the temperature was raised to 200 °C and maintained for 45 min. The solution changed from dark yellow, colorless to brown and changed to golden color finally. After that, the above solution was cooled down to

DOI: 10.1021/acsami.9b15600
ACS Appl. Mater. Interfaces XXXX, XXX, XXX−XXX

allow the precipitation of the AuMPs, centrifugation (8000 rpm, 3 min) and washing with ethanol was carried out to collect them. The as-made AuMPs were dispersed in ethanol (10 mL) finally. The preparation of the AuMPs with 60 ± 20 nm thickness was proceeded in a similar way with 256 mg PVP added, instead of 512 mg.

Calcination of AuMPs. The as-made AuMPs were deposited on clean Si wafer, followed by sonication for 5 s to remove stacked AuMPs and superfluous surfactant. For each group, 25 pieces of AuMPs were chosen unbiased and marked under optical microscope of AFM. AFM images of them were taken before and after calcination at a certain temperature. The heating rate for all of the samples is 5 °C/min.

Electrochemical Catalysis Study. For the preparation of WAuMPs, surfactant-free AuMPs and as-made AuMPs-modified glassy carbon electrodes, the WAuMPs, surfactant-free AuMPs, and as-made AuMPs were dispersed in ethanol with a concentration of 2 mg mL^{-1}. Commercial glassy carbon electrodes were polished by using 0.3 μm alumina slurries followed by 0.05 μm ones, subsequently cleaned by water. The glassy carbon electrodes were modified by drop casting of the Au ethanolic solution (10 μL) and dried naturally. Later, 2 μL of Nafion solution (5 wt %) was drop casted on the electrodes and dried naturally. For each electrode, the CV in 0.1 M KOH was measured, and its surface area could be calculated from the following equation

$$S = \frac{A}{r \times k}$$

where S is the calculated surface area; A is the consumed charge of the Au oxide reduction in 0.1 M KOH, which can be estimated by the integrated area of the reduction wave (Figure S21); r is the scan rate, which is 10 mV s^{-1} throughout our experiment; k represents consumed charge for a clean Au electrode, which reported to be 400 μC cm^{-2}.[43,44]

Characterization. Low- and HRAFM were done on a CombiScope-1000SPM and SPM SmartSPM-1000 system (AIST-NT-HORIBA), respectively. Unless mentioned in the text, the AFM images taken in our work are low-resolution AFM images. The resolution for low- and HRAFM images are 60−120 and 3−20 nm/pixel, respectively. TEM, selected area electron diffraction, and high-resolution TEM (HRTEM) were carried out by using an FEI electron microscope (Tecnai G2 F20 ST, 200 kV). SEM imaging was performed by using a JEOL scanning electron microscope (JSM-7500F, 5 kV). The absorption spectra were taken on a Hitachi UV−Vis−NIR spectrophotometer (U-4100). Electrochemical measurements were conducted on a CHI electrochemical workstation (CHI 700e) with a three-electrode cell. A glassy carbon electrode (4 mm in diameter), a platinum electrode, and a Ag/AgCl electrode (3 M NaCl) was used as the working, auxiliary, and reference electrode, respectively. UV-ozone treatment (1 h) was performed by using a commercial UV−ozone cleaner (Ossila) to obtain surfactant-free AuMPs.

■ ASSOCIATED CONTENT

Supporting Information

The Supporting Information is available free of charge on the ACS Publications website at DOI: 10.1021/acsami.9b15600.

AFM images of reshaping at 300, 400, and 500 °C; SEM images; optical images; HRTEM images; CV in the absence of methanol (PDF)

■ AUTHOR INFORMATION

Corresponding Author

*E-mail: dkurouski@tamu.edu.

ORCID

Rui Wang: 0000-0002-9452-9241

Dmitry Kurouski: 0000-0002-6040-4213

Notes

The authors declare no competing financial interest.

■ ACKNOWLEDGMENTS

The work was supported by the startup funds from Texas A&M University. We also acknowledge the TAMU Materials Characterization Facility for SEM operation. Dr. Hansoo Kim from the Microscopy and Imaging Center of TAMU is acknowledged.

■ REFERENCES

(1) Liu, J.; Yu, M.; Zhou, C.; Yang, S.; Ning, X.; Zheng, J. Passive Tumor Targeting of Renal-Clearable Luminescent Gold Nanoparticles: Long Tumor Retention and Fast Normal Tissue Clearance. *J. Am. Chem. Soc.* **2013**, *135*, 4978−4981.

(2) Liu, C.-L.; Ho, M.-L.; Chen, Y.-C.; Hsieh, C.-C.; Lin, Y.-C.; Wang, Y.-H.; Yang, M.-J.; Duan, H.-S.; Chen, B.-S.; Lee, J.-F.; Hsiao, J.-K.; Chou, P.-T. Thiol-Functionalized Gold Nanodots: Two-Photon Absorption Property and Imaging in Vitro. *J. Phys. Chem. C* **2009**, *113*, 21082−21089.

(3) Zavaleta, C. L.; Smith, B. R.; Walton, I.; Doering, W.; Davis, G.; Shojaei, B.; Natan, M. J.; Gambhir, S. S. Multiplexed Imaging of Surface Enhanced Raman Scattering Nanotags in Living Mice Using Noninvasive Raman Spectroscopy. *Proc. Natl. Acad. Sci. U.S.A.* **2009**, *106*, 13511−13516.

(4) Yang, J.; Shen, D.; Zhou, L.; Li, W.; Li, X.; Yao, C.; Wang, R.; El-Toni, A. M.; Zhang, F.; Zhao, D. Spatially Confined Fabrication of Core−Shell Gold Nanocages@ Mesoporous Silica for Near-Infrared Controlled Photothermal Drug Release. *Chem. Mater.* **2013**, *25*, 3030−3037.

(5) Wang, R.; Zhou, L.; Wang, W.; Li, X.; Zhang, F. Vivo Gastrointestinal Drug-Release Monitoring through Second Near-Infrared Window Fluorescent Bioimaging with Orally Delivered Microcarriers. *Nat. Commun.* **2017**, *8*, 14702.

(6) Li, X.; Zhao, T.; Lu, Y.; Wang, P.; El-Toni, A. M.; Zhang, F.; Zhao, D. Degradation-Restructuring Induced Anisotropic Epitaxial Growth for Fabrication of Asymmetric Diblock and Triblock Mesoporous Nanocomposites. *Adv. Mater.* **2017**, *29*, 1701652.

(7) Dai, Q.; Ouyang, M.; Yuan, W.; Li, J.; Guo, B.; Lan, S.; Liu, S.; Zhang, Q.; Lu, G.; Tie, S.; Deng, H.; Xu, Y.; Gu, M. Encoding Random Hot Spots of a Volume Gold Nanorod Assembly for Ultralow Energy Memory. *Adv. Mater.* **2017**, *29*, 1701918.

(8) Ben-Shahar, Y.; Philbin, J. P.; Scotognella, F.; Ganzer, L.; Cerullo, G.; Rabani, E.; Banin, U. Charge Carrier Dynamics in Photocatalytic Hybrid Semiconductor−Metal Nanorods: Crossover from Auger Recombination to Charge Transfer. *Nano Lett.* **2018**, *18*, 5211−5216.

(9) Liu, P.; Qin, R.; Fu, G.; Zheng, N. Surface Coordination Chemistry of Metal Nanomaterials. *J. Am. Chem. Soc.* **2017**, *139*, 2122−2131.

(10) Zhu, X.; Jia, H.; Zhu, X.-M.; Cheng, S.; Zhuo, X.; Qin, F.; Yang, Z.; Wang, J. Selective Pd Deposition on Au Nanobipyramids and Pd Site-Dependent Plasmonic Photocatalytic Activity. *Adv. Funct. Mater.* **2017**, *27*, 1700016.

(11) Kurouski, D.; Large, N.; Chiang, N.; Henry, A.-I.; Seideman, T.; Schatz, G. C.; Van Duyne, R. P. Unraveling the Near-and Far-Field Relationship of 2D Surface-Enhanced Raman Spectroscopy Substrates Using Wavelength-Scan Surface-Enhanced Raman Excitation Spectroscopy. *J. Phys. Chem. C* **2017**, *121*, 14737−14744.

(12) Lu, W.; Jiang, N.; Wang, J. Active Electrochemical Plasmonic Switching on Polyaniline-Coated Gold Nanocrystals. *Adv. Mater.* **2017**, *29*, 1604862.

(13) Millstone, J. E.; Hurst, S. J.; Métraux, G. S.; Cutler, J. I.; Mirkin, C. A. Colloidal Gold and Silver Triangular Nanoprisms. *Small* **2009**, *5*, 646−664.

(14) Yang, J.; Zhang, F.; Chen, Y.; Qian, S.; Hu, P.; Li, W.; Deng, Y.; Fang, Y.; Han, L.; Luqman, M.; Zhao, D. Core-shell Ag@ SiO 2@

DOI: 10.1021/acsami.9b15600
ACS Appl. Mater. Interfaces XXXX, XXX, XXX−XXX

mSiO2 Mesoporous Nanocarriers for Metal-Enhanced Fluorescence. *Chem. Commun.* **2011**, *47*, 11618−11620.
(15) Zhang, L.; Niu, W.; Xu, G. Synthesis and Applications of Noble Metal Nanocrystals with High-Energy Facets. *Nano Today* **2012**, *7*, 586−605.
(16) Zhou, K.; Li, Y. Catalysis Based on Nanocrystals with Well-Defined Facets. *Angew. Chem., Int. Ed.* **2012**, *51*, 602−613.
(17) Li, Y.; Liu, Q.; Shen, W. Morphology-Dependent Nanocatalysis: Metal Particles. *Dalton Trans.* **2011**, *40*, 5811−5826.
(18) Gilroy, K. D.; Elnabawy, A. O.; Yang, T.-H.; Roling, L. T.; Howe, J.; Mavrikakis, M.; Xia, Y. Thermal Stability of Metal Nanocrystals: An Investigation of The Surface and Bulk Reconstructions of Pd Concave Icosahedra. *Nano Lett.* **2017**, *17*, 3655−3661.
(19) DeSantis, C. J.; Huang, D.; Zhang, H.; Hogan, N. J.; Zhao, H.; Zhang, Y.; Manjavacas, A.; Zhang, Y.; Chang, W.-S.; Nordlander, P.; Link, S.; Halas, N. J. Laser-Induced Spectral Hole-Burning Through A Broadband Distribution of Au Nanorods. *J. Phys. Chem. C* **2016**, *120*, 20518−20524.
(20) Albrecht, W.; Deng, T.-S.; Goris, B.; van Huis, M. A.; Bals, S.; van Blaaderen, A. Single Particle Deformation and Analysis of Silica-Coated Gold Nanorods Before and After Femtosecond Laser Pulse Excitation. *Nano Lett.* **2016**, *16*, 1818−1825.
(21) Zhou, X.; Li, X. Y.; Lu, K. Enhanced Thermal Stability of Nanograined Metals Below A Critical Grain Size. *Science* **2018**, *360*, 526−530.
(22) Kurouski, D.; Large, N.; Chiang, N.; Greeneltch, N.; Carron, K. T.; Seideman, T.; Schatz, G. C.; Van Duyne, R. P. Unraveling Near-Field and Far-Field Relationships for 3D SERS Substrates−A Combined Experimental and Theoretical Analysis. *Analyst* **2016**, *141*, 1779−1788.
(23) Teranishi, T.; Hasegawa, S.; Shimizu, T.; Miyake, M. Heat-Induced Size Evolution of Gold Nanoparticles in the Solid State. *Adv. Mater.* **2001**, *13*, 1699−1701.
(24) Dai, Y.; Lu, P.; Cao, Z.; Campbell, C. T.; Xia, Y. The Physical Chemistry and Materials Science Behind Sinter-Resistant Catalysts. *Chem. Soc. Rev.* **2018**, *47*, 4314−4331.
(25) Yuan, W.; Zhang, D.; Ou, Y.; Fang, K.; Zhu, B.; Yang, H.; Hansen, T. W.; Wagner, J. B.; Zhang, Z.; Gao, Y.; Wang, Y. Direct In Situ TEM Visualization and Insight into the Facet-Dependent Sintering Behaviors of Gold on TiO2. *Angew. Chem., Int. Ed.* **2018**, *57*, 16827−16831.
(26) Goswami, G. K.; Nanda, K. K. Size-Dependent Melting of Finite-Length Nanowires. *J. Phys. Chem. C* **2010**, *114*, 14327−14331.
(27) Lee, J.; Lee, J.; Tanaka, T.; Mori, H. In Situ Atomic-Scale Observation of Melting Point Suppression in Nanometer-Sized Gold Particles. *Nanotechnology* **2009**, *20*, 475706.
(28) Hansen, T. W.; DeLaRiva, A. T.; Challa, S. R.; Datye, A. K. Sintering of Catalytic Nanoparticles: Particle Migration or Ostwald Ripening? *Acc. Chem. Res.* **2013**, *46*, 1720−1730.
(29) Campbell, C. T.; Parker, S. C.; Starr, D. E. The Effect of Size-Dependent Nanoparticle Energetics on Catalyst Sintering. *Science* **2002**, *298*, 811−814.
(30) Campbell, C. T. The Energetics of Supported Metal Nanoparticles: Relationships to Sintering Rates and Catalytic Activity. *Acc. Chem. Res.* **2013**, *46*, 1712−1719.
(31) Sun, X.; Dong, S.; Wang, E. Large-Scale Synthesis of Micrometer-Scale Single-Crystalline Au Plates of Nanometer Thickness by a Wet-Chemical Route. *Angew. Chem.* **2004**, *116*, 6520−6523.
(32) Li, C. C.; Cai, W. P.; Cao, B. Q.; Sun, F. Q.; Li, Y.; Kan, C. X.; Zhang, L. D. Mass Synthesis of Large, Single-Crystal Au Nanosheets based on a Polyol Process. *Adv. Funct. Mater.* **2006**, *16*, 83−90.
(33) Cheng, Y.; Qiu, C.; Ma, H.; Zhang, X.; Gu, X. Unusual Corrosion Process of Gold Nanoplates and the Mechanism Study. *Nanoscale* **2010**, *2*, 685−688.
(34) Kan, C.; Wang, G.; Zhu, X.; Li, C.; Cao, B. Structure and Thermal Stability of Gold Nanoplates. *Appl. Phys. Lett.* **2006**, *88*, 071904.
(35) Kan, C.; Zhu, X.; Wang, G. Single-Crystalline Gold Microplates: Synthesis, Characterization, and Thermal Stability. *J. Phys. Chem. B* **2006**, *110*, 4651−4656.
(36) Radha, B.; Kulkarni, G. A Real Time Microscopy Study of the Growth of Giant Au Microplates. *Cryst. Growth Des.* **2011**, *11*, 320−327.
(37) Wang, R.; Kurouski, D. Elucidation of Tip-Broadening Effect in Tip-Enhanced Raman Spectroscopy (TERS): A Cause of Artifacts or Potential for 3D TERS. *J. Phys. Chem. C* **2018**, *122*, 24334−24340.
(38) Švorčík, V.; Kvítek, O.; Lyutakov, O.; Siegel, J.; Kolská, Z. Annealing of Sputtered Gold Nano-Structures. *Appl. Phys. A* **2011**, *102*, 747−751.
(39) Millstone, J. E.; Park, S.; Shuford, K. L.; Qin, L.; Schatz, G. C.; Mirkin, C. A. Observation of a Quadrupole Plasmon Mode for a Colloidal Solution of Gold Nanoprisms. *J. Am. Chem. Soc.* **2005**, *127*, 5312−5313.
(40) Qin, Y.; Song, Y.; Sun, N.; Zhao, N.; Li, M.; Qi, L. Ionic Liquid-Assisted Growth of Single-Crystalline Dendritic Gold Nanostructures with a Three-Fold Symmetry. *Chem. Mater.* **2008**, *20*, 3965−3972.
(41) Wang, L.; Wu, X.; Li, X.; Wang, L.; Pei, M.; Tao, X. Facile Synthesis of Concave Gold Nanoplates in Hexagonal Liquid Crystal Made of SDS/Water System. *Chem. Commun.* **2010**, *46*, 8422−8423.
(42) Jena, B. K.; Raj, C. R. Synthesis of Flower-Like Gold Nanoparticles and Their Electrocatalytic Activity towards the Oxidation of Methanol and the Reduction Of Oxygen. *Langmuir* **2007**, *23*, 4064−4070.
(43) Angerstein-Kozlowska, H.; Conway, B. E.; Hamelin, A.; Stoicoviciu, L. Elementary Steps of Electrochemical Oxidation of Single-Crystal Planes of Au Part II. A Chemical and Structural Basis of Oxidation of the (111) Plane. *J. Electroanal. Chem. Interfacial Electrochem.* **1987**, *228*, 429−453.
(44) Trasatti, S.; Petrii, O. A. Real Surface Area Measurements in Electrochemistry. *Pure Appl. Chem.* **1991**, *63*, 711−734.

DOI: 10.1021/acsami.9b15600
ACS Appl. Mater. Interfaces XXXX, XXX, XXX−XXX